Chemical Engineering Journal 524 (2025) 169730

Contents lists available at ScienceDirect

Chemical Engineering Journal

journal homepage: www.elsevier.com/locate/cej

Scalable electrode substrates for environmentally stable and flexible humidity sensors

Zhenyu Gong [a,b,1], Zibo Chen [a,b,1], Fangzheng Xi [a,b,1], Bo Liu [a,c,d,*], Yunfa Si [a,b], Jie Wen [a,b], Xiaodong Ji [a,b], Mingyang Tanwei [a,b], Cheng Chen [a,e], Peng Li [c], Shaowen Cao [b], Geng Wu [a,*], Daping He [a,b,c,d,*]

[a] Sanya Science and Education Innovation Park of Wuhan University of Technology, Sanya, 572000, China
[b] School of Materials Science and Engineering, Wuhan University of Technology, Wuhan, 430070, China
[c] School of Physics and Mechanics, Wuhan University of Technology, Wuhan, China
[d] Hubei Engineering Research Center of RF-Microwave Technology and Application, School of Physics and Mechanics, Wuhan University of Technology, Wuhan, 430070, China
[e] State Key Laboratory of Advanced Technology for Materials Synthesis and Processing, Wuhan University of Technology, Wuhan, 430070, China

ARTICLE INFO

Keywords:
Scalable electrode substrates
Environmental stability
Flexibility
Graphene film
Humidity sensors

ABSTRACT

Environmental stability and mechanical flexibility are essential for practical humidity sensors, yet conventional electrode substrates often fail to simultaneously meet the demands of high conductivity, chemical resistance, flexibility, and scalable fabrication. Herein, we report a hundred-meter-scale production of macroscopic graphene film (GF) via sequential high-temperature annealing and roll pressing, enabling its direct use as high-performance electrode substrates. Through laser patterning, GF is transformed into interdigital electrodes (GF-IDEs) with ultrahigh conductivity (1.1×10^6 S m^{-1}), exceptional flexibility, and outstanding resistance to acid, alkali, and salt spray corrosion. By integrating a conformal ~150 nm graphene oxide (GO) layer, we construct an all-carbon humidity sensor featuring high sensitivity, rapid response/recovery, and superior performance compared to state-of-the-art GO-based sensors using traditional electrode substrates. Notably, the device retains over 99 % of its performance after 500 bending cycles or 48 h of salt spray exposure. This robust sensor enables real-time monitoring of human respiration, contactless human-machine interaction, and dynamic plant transpiration, demonstrating its broad potential for wearable and environmental sensing applications.

1. Introduction

Humidity sensors are integral to emerging technologies such as the Internet of Things, smart electronics, environmental monitoring, and modern agriculture [1–4]. To meet the demands of these diverse scenarios, sensors must offer not only high sensitivity but also excellent environmental stability and mechanical flexibility [5,6]. Electrochemical humidity sensors, composed of humidity-sensitive receptors and electrode substrates as transducers, offer key advantages in detection range, signal processing, and cost-effectiveness [7]. While extensive efforts have focused on optimizing humidity-sensitive materials to improve sensitivity, practical applicability is increasingly limited by inadequate environmental adaptability—primarily dictated by the substrate material [8,9]. Conventional substrates, including metal electrodes and silver nanowire/polymer composites [10,11], often suffer from high cost, limited flexibility, poor corrosion resistance, and complex processing, collectively restricting sensor reliability and scalability [12–14]. Despite its critical role, the design and exploration of novel substrate materials remain insufficient, significantly hindering the rational development of next-generation humidity sensors.

To address these limitations, the selection of electrode substrates with high conductivity, mechanical flexibility, chemical stability, and environmental resilience is essential. Graphene, featuring a unique single-layer sp^2 hybrid carbon atom honeycomb lattice structure [15–19], exhibits exceptional structural stability and resistance to chemical corrosion, withstanding harsh conditions such as strong acids, alkalis, and high salt spray environments [20–24]. Moreover, graphene exhibits favorable biocompatibility [25,26], making it an attractive

* Corresponding authors at: Sanya Science and Education Innovation Park of Wuhan University of Technology, Sanya, 572000, China.
E-mail addresses: liubo2024@whut.edu.cn (B. Liu), gengwu@mail.ustc.edu.cn (G. Wu), hedaping@whut.edu.cn (D. He).
[1] Zhenyu Gong, Zibo Chen and Fangzheng Xi contributed equally to this work.

https://doi.org/10.1016/j.cej.2025.169730
Received 28 July 2025; Received in revised form 9 October 2025; Accepted 15 October 2025
Available online 17 October 2025

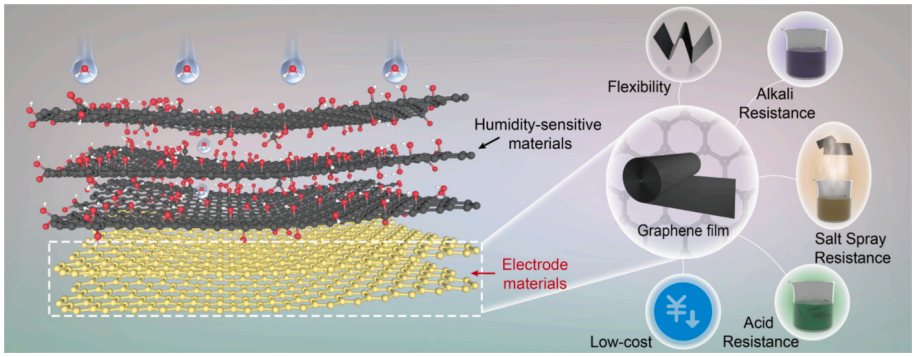

Fig. 1. Various outstanding characteristics of GF as an electrode substrate for humidity sensors.

candidate for constructing high-performance humidity sensor electrodes. However, graphene is currently predominantly utilized in the powder state [27–29]. Its macroscopic applications face substantial challenges due to the difficulties in achieving homogeneous and stable dispersion, alongside the formidable complexity of controlling flake orientation [30]. These limitations severely impede its widespread adoption in transducers. Laser-induced graphene (LIG) is a representative graphene material and has been widely used in humidity sensors [31–33]. However, their conductivity (approximately 1253 S m^{-1}) [34] falls significantly below that of conventional metal electrodes (>10^6 S m^{-1}), leading to decreased signal transmission efficiency. Furthermore, the high-energy laser irradiation used in LIG processing often induces non-equilibrium carbon atom rearrangement, generating topological defects and amorphous domains [35]. These structural disruptions impair the integrity of the ideal graphene lattice, diminishing mechanical strength and interlayer cohesion. As a result, the flexibility and long-term reliability of LIG electrodes are severely compromised. Chemical vapor deposition method is currently a common approach for producing high-quality graphene films. However, its high cost and challenges in large-scale fabrication significantly limit the macroscale production of graphene films. Therefore, the development of graphene-based electrode substrates with enhanced conductivity, structural integrity, mechanical durability, and environmental resilience is urgently needed to meet the performance demands of next-generation humidity sensors. Interestingly, the high-temperature annealing process can rearrange carbon atoms within graphene, forming a highly ordered sp^2 hybridized carbon crystal structure. This notably enhances electrical conductivity and structural integrity, making large-scale production of high-performance graphene electrodes possible. Table S1 compares the significant advantages of GF over other graphene materials in terms of scalability, conductivity, and mechanical durability.

Herein, we report the scalable fabrication of macroscopic graphene film (GF) at the hundred-meter scale from graphene oxide (GO) slurry via sequential thermal annealing and subsequent roller pressing. Leveraging this high-quality GF, laser patterning was employed to fabricate GF-based interdigitated electrodes (GF-IDEs) as transducers for large-scale production. The resulting GF-IDEs exhibit excellent cost-effectiveness, ultrahigh conductivity (1.1×10^6 S m^{-1}), outstanding flexibility, and superior chemical stability under acid, alkali, and salt spray corrosion conditions (Fig. 1). Based on these GF-IDEs, an electrochemical impedance-type humidity sensor (GF-GO) was constructed using GO as the humidity-sensitive layer. The sensor demonstrates exceptional performance, featuring high sensitivity and rapid response/recovery times, outperforming state-of-the-art GO-based humidity sensors with conventional electrode substrates. More importantly, the sensor maintains over 99 % of its performance after 500 bending cycles and 48 h of salt spray exposure, highlighting its environmental resilience and mechanical durability. Leveraging these attributes, GF-GO has been effectively applied in diverse scenarios such as human respiratory monitoring, non-contact sensing, and plant growth monitoring. This work underscores the potential of GF as a next-generation substrate, overcoming the limitations of conventional materials in environmental stability and mechanical flexibility.

2. Experimental section

2.1. Materials

GO used in this work was obtained from Sanya Hanxi Graphene Institute Technology Co., Ltd. Chemical reagents including LiCl, CH_3COOK, $MgCl_2$, K_2CO_3, NaBr, NaCl, KCl, KNO_3, and K_2SO_4 were purchased from Macklin.

2.2. Fabrication of macroscopic graphene films

GF were prepared from GO via thermal reduction. First, GO was dispersed in deionized water to form a 4 wt% suspension. This GO suspension was then converted into a GO colloid through mechanical stirring, followed by coating to form a GO film. Under an argon atmosphere, the GO film was gradually heated to 1300 °C and held for 2 h, yielding an amorphous carbon film. Subsequently, the carbonized structure was annealed at 2850 °C for 1 h in argon to form a fully sp^2-hybridized graphitic structure. Finally, the sample was roll-pressed at 200 MPa to obtain a dense graphene film.

2.3. Fabrication of GF-GO humidity sensor

The GF was patterned using a laser scribing micromachining system controlled by a computer-guided laser engraver (ProtoLaser U4, LPKF Laser & Electronics AG, Slovenia). The patterning parameters were set as follows: power supply frequency of 100 kHz, laser power of 1.85 W, structuring speed of 100 mm/s, focus compensation of 0.05 mm, and 5 repetitions. The IDE dimensions were designed with a width of 6.0 mm, length of 11.25 mm, five electrode pairs, finger length of 5 mm, finger width of 500 μm, and electrode spacing of 250 μm. A 50 μL aliquot of 0.02 wt% GO solution was drop-casted onto the GF-IDEs, followed by drying at 50 °C for 12 h to form a uniform GO film.

3. Material characterization of humidity sensor

HRTEM samples were prepared by ion milling at −80 °C to a thickness of less than 100 nm. HRTEM images were acquired using a JEOL-F200 instrument. Scanning electron microscope (SEM) imaging was conducted on a Zeiss Crossbeam 350 dual-beam microscope. X-ray photoelectron spectroscopy (XPS) analyses employed an Al monochromatic X-ray source (25.0 W, 100.0 μm spot size). Charge neutralizer settings were 0.3 V and 5.0 μA, with analyses performed in FAT mode. High-resolution C 1 s and O 1 s spectra were acquired under identical parameters (pass energy: 112 eV, step size: 0.1 eV). Charge correction referenced the C 1 s peak to 284.8 eV. Fourier transform infrared (FTIR)

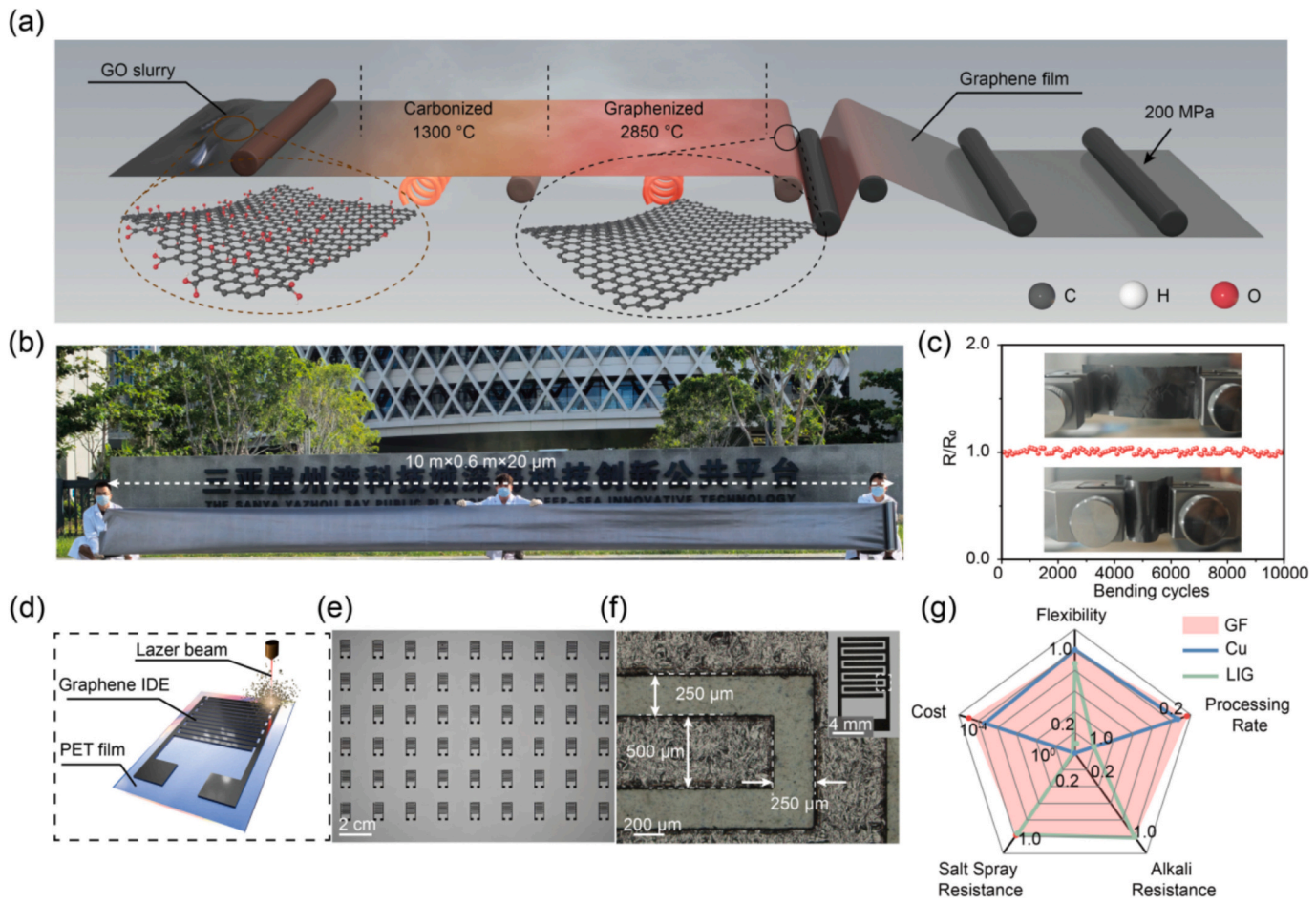

Fig. 2. (a) Schematic illustration of the GF fabrication process. (b) Optical photograph of a representative GF sample. (c) Resistance changes of GF after 10,000 bending cycles. (d) Schematic diagram of laser processing IDEs on GF. (e) Optical image showing large-scale fabrication of IDEs. (f) Optical photograph of the IDE. (g) Radar chart comparing GF, Cu, and LIG in terms of cost, flexibility, processing rate, alkali corrosion resistance, and salt spray corrosion resistance.

spectroscopy was recorded in ATR mode using a Nicolet 60-SXB IR spectrometer. Static contact angles were measured via the sessile drop method (KRÜSS Scientific DSA30B); images were captured upon stabilization of deionized water droplets, and angles were automatically fitted using dedicated software. X-ray diffraction (XRD) patterns were obtained on a Rigaku Smartlab diffractometer using Cu Kα radiation (λ = 1.5406 Å) at a scan rate of 10° min^{-1}. White light interferometry (WLI) profiles were measured using a Bruker Contour X-200 system equipped with a green light source. Raman spectroscopy utilized 532 nm laser excitation.

3.1. Humidity sensor testing system

Controlled relative humidity (RH) environments (11 %, 23 %, 33 %, 43 %, 59 %, 75 %, 84 %, 93 %, 97 % RH) were generated at room temperature using saturated salt solutions (LiCl, CH_3COOK, $MgCl_2$, K_2CO_3, NaBr, NaCl, KCl, KNO_3, K_2SO_4) and calibrated with a commercial hygrometer (Testo 605-H1). Plant transpiration monitoring was conducted using *Epipremnum aureum* (pothos). All electrical measurements were performed using an electrochemical workstation (CHI 660E, Shanghai, China). Humidity response testing was conducted using the AC impedance-time method with the following parameters: initial voltage of 0 V, bias voltage of 0.025 V, frequency of 100 Hz, and sampling interval of 1 s. For Electrochemical Impedance Spectroscopy testing, parameters included an initial voltage of 0 V, bias voltage of 0.025 V, and a frequency sweep range of 1–100,000 Hz.

4. Results and discussion

The highly conductive and flexible GF was fabricated through high-temperature annealing of GO. A schematic illustration of the preparation process is presented in Fig. 2a. Starting with GO slurry, the material was subjected to sequential carbonization and graphitization treatments at 1300 °C and 2850 °C, respectively. Subsequently, the GF was continuously formed on a PET substrate via a rolling process. Fig. 2b displays representative photographs of the as-prepared GF (measuring 10 m × 0.6 m × 20 μm), confirming the successful large-scale production of GF itself. Fig. 2c and video S1 display the resistance change of the GF after 10,000 bending cycles. Evidently, no significant resistance variation occurs, which is attributable to graphene's unique microstructure [17]. Its hexagonally arranged two-dimensional structure, coupled with strong intermolecular forces, enables it to withstand substantial deformation without fracture under large-range bending. Figs. S1–2 confirms the successful preparation of highly crystalline GF. Considering laser patterning as an efficient method for rapid processing, it is suitable for structuring the GF to serve as the electrode substrate. Fig. 2d illustrates the process of laser patterning the GF into IDEs. This approach clearly enables the scalable fabrication of GF-IDEs, as demonstrated in Fig. 2e. An optical image of the laser-patterned electrode is shown in Fig. 2f, detailing its geometry: finger width of 500 μm and gap spacing of 250 μm.

More compellingly, the GF exhibits superior characteristics compared to traditional metal materials (using Cu as an example) and LIG, as summarized in Fig. 2g. Firstly, regarding flexibility, the GF

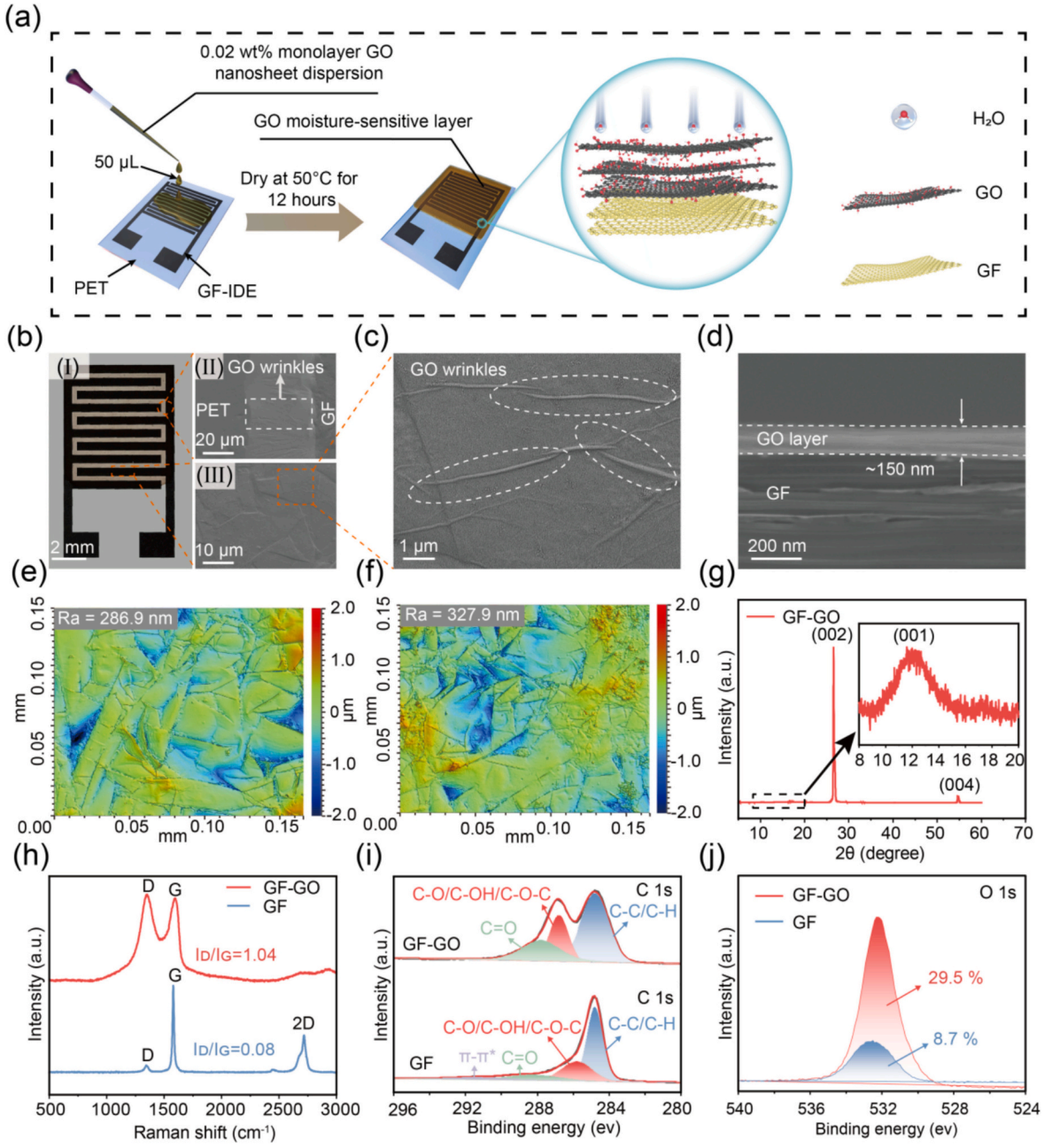

Fig. 3. (a) Schematic illustration of the GF-GO sensor fabrication. (b) Surface morphology of the GF-GO sensor: (I) Optical photograph of the GF-GO sensor; (II) SEM image of the GF/PET step region in the GF-GO sensor; (III) Surface SEM morphology of the GF in the GF-GO sensor. (c) Magnified view of the rectangular area in (III). (d) Cross-sectional SEM image of the GF-GO sensor (GO layer thickness ≈150 μm). (e) WLI image of the GF surface. (f) WLI image of the GF-GO surface. (g) XRD pattern of GF-GO. (h) Raman spectra comparison of GF and GF-GO. High-resolution XPS spectra of C 1 s (i) and O 1 s (j) for GF and GF-GO.

demonstrates exceptional bendability. In stark contrast, LIG, also a carbon-based material, suffers a significant conductivity loss of 15.6 % after only 500 bending cycles (Fig. S3). Secondly, the GF also possesses outstanding corrosion resistance. Following 48 h of salt spray corrosion and 7 days of exposure to 1 M KOH, no substantial decline in conductivity is observed (Figs. S4-S5). Conversely, Cu undergoes severe surface corrosion and experiences a drastic drop in conductivity to merely 0.11 S m^{-1} under identical conditions. Furthermore, in terms of cost-effectiveness and processing speed, the GF demonstrates lower costs and faster fabrication rates compared to both Cu and LIG (Table S2). Based on these results, the GF presents significantly greater promise than conventional materials for large-scale industrial applications.

Fig. 3a schematically illustrates the fabrication process of the all-carbon-based humidity sensor, utilizing GO (flake size distribution shown in Fig. S6) as the humidity-sensitive material and GF as the electrode substrate. A 50 μL of GO solution was drop-casted onto the GF electrode surface to ensure uniform coverage, followed by drying to form a homogeneous GO film-coated GF humidity sensor. An optical image in Fig. 3b(I) demonstrates the uniform coating of GO over the GF electrode substrate, revealing a yellowish-brown film covering the interdigital electrodes. To gain deeper insights into the morphology of GO on the GF surface, SEM characterization was performed. Notably, as shown in Fig. 3b(II), at the GF-PET interface step, the GO film does not break but instead forms an inclined GO film bridging the step, confirming its continuous and conformal coverage over the entire electrode substrate. Fig. 3b(III) further displays the surface morphology of GO on GF, showing the interdigital regions remaining smooth. Higher magnification imaging reveals characteristic wrinkles in the GO film deposited

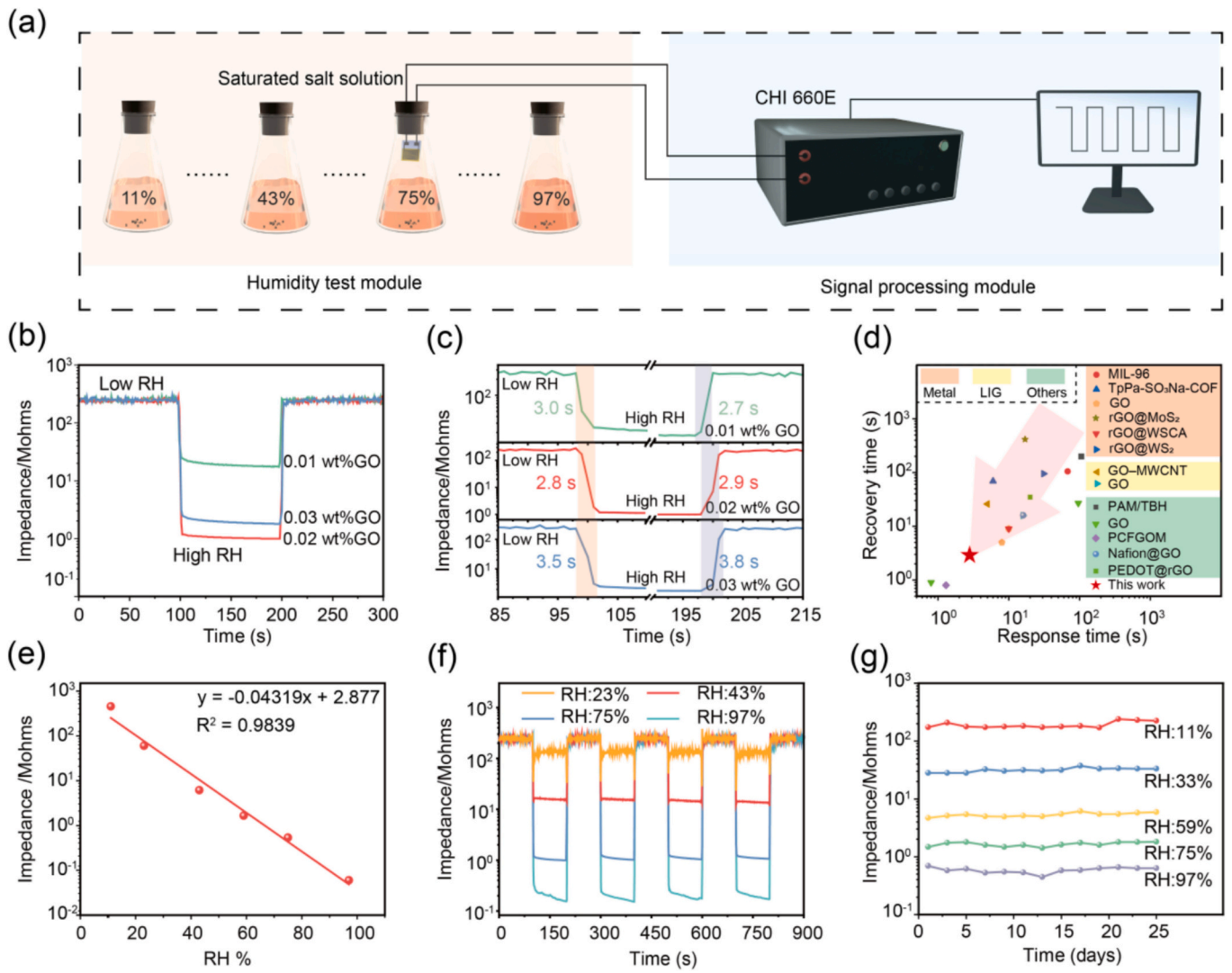

Fig. 4. (a) Schematic demonstration of the GF-GO sensor performance testing. (b) Sensitivity comparison of GF-GO sensors with different GO concentrations. (c) Response/recovery time comparison. (d) Response/recovery time comparison between the GF-GO sensor and previously reported GO-based humidity sensors utilizing different electrode substrates. (e) Linear correlation of the GF-GO sensor within 11 %–97 % RH. (f) Repeatability and (g) long-term stability of the GF-GO sensor at different humidity levels.

on the GF, providing direct evidence of GO coverage. Crucially, the underlying GF wrinkles remain visible through the GO film (Fig. 3c), indicating its ultrathin nature. To quantify the GO film thickness, cross-sectional SEM analysis was conducted (Fig. 3d and Fig. S7). The results show an ultrathin GO layer (approximately 150 nm thick) intimately adhering to the GF. This reduced thickness facilitates the rapid absorption and desorption of water molecules within the film, laying the foundation for the sensor's ultrafast response and recovery. Additionally, the surface morphology was characterized using WLI. The arithmetic mean roughness (Ra) of the pristine GF surface, depicted in Fig. 3e, was measured to be 286.9 nm, indicating a relatively smooth surface. In comparison, the Ra value for the GF-GO composite surface increased slightly to 327.9 nm (Fig. 3f), attributable to the wrinkles introduced by the conformal GO coating. Structural information for Cu and LIG substrates is provided in Figs. S8-S11.

To further investigate the structural and chemical properties of the GF-GO composite, XRD, Raman spectroscopy, and Fourier transform infrared (FTIR) spectroscopy were employed. The XRD pattern of pristine GF (Fig. S12) exhibits two sharp diffraction peaks at ~26.5° and ~54.7°, corresponding to the (002) and (004) crystal planes, respectively. In contrast [36], the XRD pattern of GF-GO (Fig. 3g), while retaining the characteristic (002) and (004) peaks of the underlying GF at 26.5° and 54.7°, displays an additional peak at ~12°. This peak is assigned to the (001) plane of GO [37], consistent with the XRD pattern of pure GO film (Fig. S13). Combined with the SEM observations, this confirms the successful integration of the GO film onto the GF substrate. Raman spectroscopy further elucidates structural differences (Fig. 3h). The GF spectrum shows a weak D-band and an intense G-band (I_D/I_G = 0.08), indicative of its high graphitization degree and excellent lattice integrity. This is corroborated by a prominent 2D-band at ~2714 cm^{-1} [38]. Conversely, the GF-GO spectrum exhibits a significantly enhanced D-band intensity (I_D/I_G = 1.04), signifying the introduction of abundant defects and oxygen-containing functional groups (e.g., hydroxyl, epoxy, carboxyl) within the surface GO film. These functional groups are crucial for conferring humidity sensitivity to GO [39]. FTIR spectroscopy was performed to identify specific functional groups in GF-GO (Fig. S14). Distinct characteristic peaks are observed at ~3500 cm^{-1} (O—H stretching), ~1730 cm^{-1} (C═O stretching of carboxyl), ~1630 cm^{-1} (C═O stretching of carbonyl), and ~ 1080 cm^{-1} (C—O stretching) [40]. These hydrophilic groups impart strong hydrophilicity to the GO film. These properties facilitate the rapid absorption/desorption of water molecules upon humidity changes, inducing significant alterations in

Table 1
Comparison of this work with various types of recent state-of-the-art humidity sensors.

Electrode materials	Humidity-sensitive materials	Sensor Type	Response time (s)	Recovery time (s)	Ref.
–	PAM/Tapioca Bulk Hydrogel	Conductance	275.6	227.0	[45]
Au	MIL-96	Capacitance	105	105	[46]
Ag-Pd	TpPa-SO_3Na-COF	Impedance	6	69	[47]
Ti_3C_2Tx MNSs	GO	Capacitance/ Impedance	0.8	0.9	[48]
–	PCFGOM	Capacitance/ Impedance	1.3	0.8	[49]
graphene LIG	GO–MWCNT	Resistance	5.0	26.0	[50]
LIG	GO	Capacitance	15.8	15.8	[33]
Au/ALN/ SiO_2	GO	SAW	10.0	9.0	[51]
Pt/SiO_2	rGO@MoS_2	Resistance	17.0	414.0	[52]
Au	GO	Impedance	8.0	5.0	[53]
Si	Nafion@GO	Voltage	16.0	16.0	[54]
PrGANPs INK	PEDOT@rGO	Resistance	20.0	35.0	[55]
AgNW Paper	GO	Current	280.0	27.0	[56]
Cu	rGO@WSCA	Resistance	10.0	9.0	[57]
Au	rGO@WS_2	Resistance	31.0	95.0	[58]
GF	GO	Impedance	2.8	2.9	This work

electrical properties, thereby enhancing the humidity sensor's sensitivity and response/recovery speed. Contact angle measurements provide direct evidence of the superior hydrophilicity of GO (Fig. S15): after GO deposition, the contact angle on the IDE dramatically decreased from 100.2° to 29.7°.

Furthermore, the surface chemical composition of the GF-GO composite was investigated using XPS. As shown in Fig. 3i, the C 1 s spectrum of pristine GF exhibits a strong, sharp peak at 284.8 eV, corresponding to the typical sp^2-hybridized carbon (C-C/C=C) in GF. Concurrently, a distinct π-π satellite peak is observed at ~291 eV for GF, originating from electron transitions within the aromatic structure [41]. In contrast, the C 1 s spectrum of GF-GO shows the disappearance of the π-π satellite peak, while peaks associated with C—O and C═O bonds are significantly enhanced. Specifically, the characteristic peak at 284.8 eV for GF-GO is assigned to C-C/C-H. The peak at 286.8 eV corresponds to C—O bonds (-C-O-C/-OH); these groups enhance the hydrophilicity of GO, providing abundant adsorption sites for water molecules. The peak at 287.8 eV is attributed to C═O bonds (-COOH). These carboxyl groups also improve the hydrophilicity of the GO sensing layer and impart higher chemical reactivity [42,43]. Supporting this analysis, quantitative oxygen content determination (Fig. 3j and Figs. S16-S17) demonstrates a significant increase from 8.7 % for pristine GF to 29.5 % for GF-GO upon integration of the GO layer, providing robust confirmation of the conclusions.

The humidity sensing performance of the GF-GO sensor was further evaluated (Fig. 4a and Fig. S18 show the schematic diagram and physical photograph of the sensor test setup, respectively). Fig. S19 compares the humidity response characteristics of GF-GO under different testing frequencies. The results indicate that at the higher frequencies, the sensor exhibits the lower sensitivity and the lower responsiveness to humidity changes. This is attributed to the polarization relaxation of water molecules being unable to keep pace with the rapid oscillation of the high-frequency electric field [44]. Notably, at 100 Hz, the sensor demonstrates the highest sensitivity and optimal linear correlation (Fig. S20). Consequently, all subsequent tests were conducted at 100 Hz. To achieve optimal sensing performance, the concentration of the GO solution was systematically varied while maintaining a fixed volume, as concentration directly alters the thickness of the humidity-sensitive layer. Figs. 4b-c illustrate the sensitivity and response/recovery times of GF-GO sensors fabricated with GO concentrations of 0.01 wt%, 0.02 wt%, and 0.03 wt%. It is evident that the sensor with a GO concentration of 0.02 wt% delivers the best overall performance: it exhibits the highest sensitivity (2920 kΩ/%RH) during transitions from low to high humidity (Fig. 4b), coupled with ultrafast response/recovery times of 2.8 s / 2.9 s (Fig. 4c). Fig. S21 demonstrates the impedance stability and capacitance stability of the GF-GO sensor, confirming the reliable performance of the humidity sensor at 100 Hz and under a concentration of 0.02 wt%. To elucidate the superior performance at 0.02 wt%, electrochemical impedance spectroscopy (EIS) and SEM characterization were performed. Fig. S22 presents the thicknesses of GO layers at different concentrations and their corresponding EIS spectra under identical humidity conditions. The results reveal GO layer thicknesses of 75 nm, 150 nm, and 250 nm for concentrations of 0.01 wt%, 0.02 wt%, and 0.03 wt %, respectively. Crucially, the sample with 0.02 wt% GO exhibits the lowest charge transfer resistance. It exhibits optimal humidity sensing performance at this thickness. Furthermore, Fig. 4d and Table 1 present a comparison of the response/recovery times of the GF-GO sensor against those of graphene oxide-based humidity sensors employing different electrode substrates, as well as other advanced flexible humidity sensors. This comparison demonstrates the superiority of the GF-GO sensor in sensing performance over those utilizing traditional metal electrodes or LIG-based substrates, highlighting its enhanced capabilities.

Fig. 4e reveals that the impedance of the GF-GO sensor decreases strikingly by over four orders of magnitude as the RH increases from 11 % to 97 %, exhibiting excellent linearity with a correlation coefficient (R^2) of 0.9839. The humidity hysteresis characteristic of GF-GO is presented in Fig. S23. Additionally, the GF-GO sensor demonstrates exceptional repeatability and long-term stability. Fig. 4f shows no significant deviation in the response amplitude during four complete sensing cycles, where RH was sequentially elevated from 11 % to target levels (23 %, 43 %, 75 %, 97 %) and then returned to 11 %, confirming its precise humidity sensing capability. Crucially, Fig. 4g indicates negligible change in impedance values across different humidity levels after 25 days, underscoring its exceptional long-term stability.

To fully validate the superiority of GF-based humidity sensors, the humidity sensing performance of Cu and LIG substrates with identical GO humidity-sensitive layers was compared within the 11 %–75 % RH range. As shown in Fig. 5a, the GF-based sensor significantly outperforms Cu- and LIG-based sensors in both sensitivity and response/recovery time. Fig. 5b displays the EIS plots of the three sensors at 75 % RH. The charge transfer resistance (Rct) of GF-GO and Cu-GO is two orders of magnitude lower than that of LIG-GO. Compared with Cu-GO, the Rct of GF-GO is only half of its value. This indicates that when GF serves as the electrode material, charges can transfer more easily through the GO layer to the electrode interface. This may be attributed to the fact that both GF and GO are carbon-based materials with similar chemical properties and crystalline structures (sp^2 carbon networks), and the presence of few functional groups on the GF surface, resulting in excellent chemical compatibility [59]. Consequently, the energy barrier for electron transfer between GF and GO is extremely low, ensuring highly efficient charge transport. These interfacial characteristics endow the GF-GO sensor with higher sensitivity and shorter response/recovery times (Fig. 5c).

To validate the environmental adaptability of the humidity sensors under different conditions, simulated salt spray corrosion tests and bending tests were conducted. The GF-GO sensor maintained exceptional humidity sensing performance even under extreme environments. After aging in a simulated salt spray environment (5 wt% NaCl solution, 48 h), the sensor exhibited sensitivity retention rates exceeding 99 % at both medium-low humidity (43 % RH) and high humidity (97 % RH), significantly outperforming the Cu-GO sensor (Fig. 5d). This superior corrosion resistance is attributed to the inherently excellent salt spray

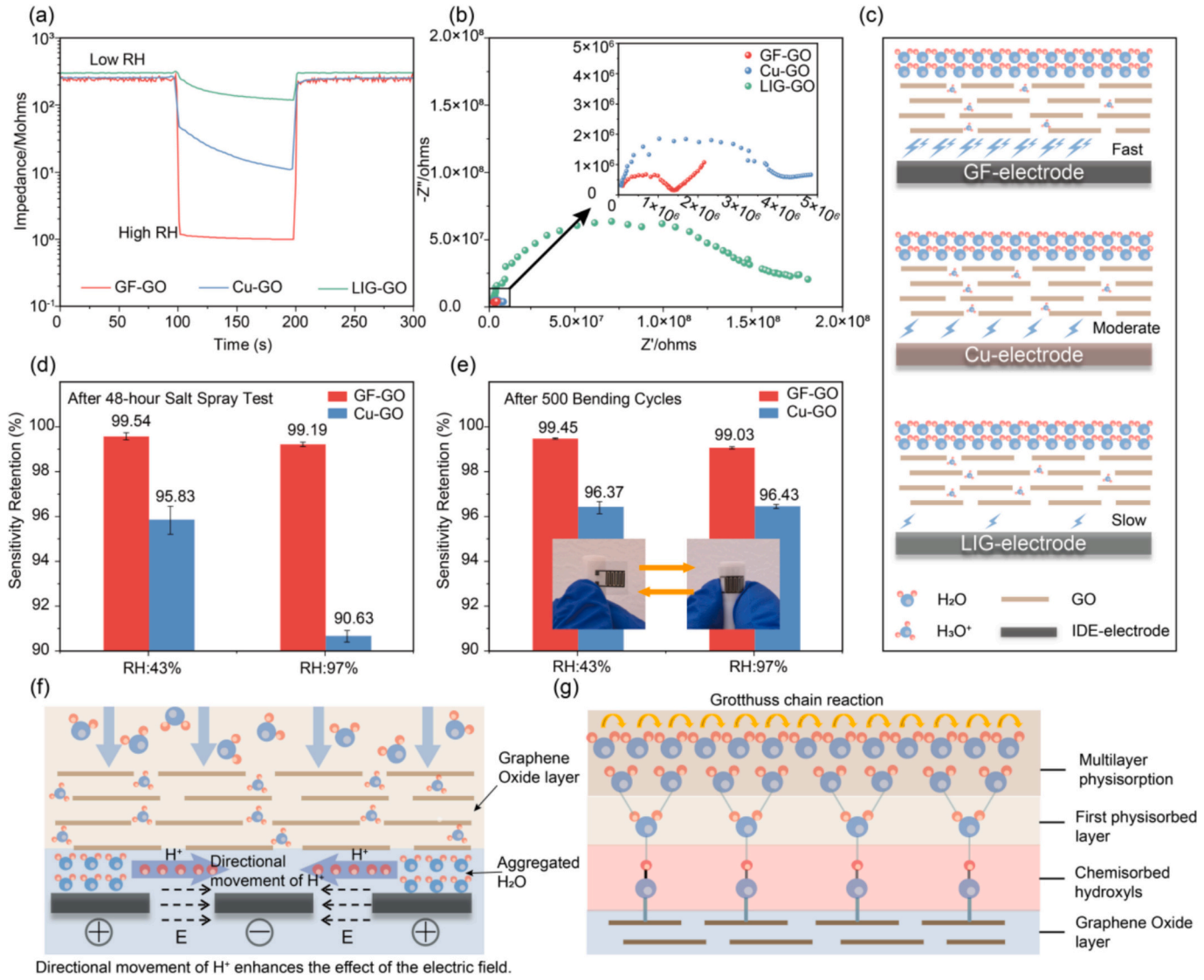

Fig. 5. (a) Humidity response curves, (b) EIS spectra, and (c) schematic illustration of the sensing mechanism for GF-GO, Cu-GO, and LIG-GO sensors. Sensitivity retention rate of GF-GO and Cu-GO sensors after (d) 48 h salt spray corrosion and (e) 500 bending cycles. (f) Schematic illustration of the mechanism for enhanced humidity response by GF. (g) Mechanism of water molecule adsorption/desorption on GO at varying humidity levels.

corrosion resistance of the GF substrate, which was further corroborated by EIS measurements (Fig. S24). Furthermore, the GF-GO sensor demonstrated outstanding flexibility. Following 500 bending cycles around a cylindrical mandrel with a 4 mm radius, its sensitivity retention rates at both medium-low and high humidity levels remained as high as 99 %, again surpassing those of the Cu-GO sensor (Fig. 5e and Fig. S25). This remarkable mechanical stability originates from the homogenous graphene structure shared by both GF and GO, which imparts stronger interfacial adhesion. These exceptional properties endow the GF-GO sensor with broad potential for applications in various flexible electronic devices.

Fig. 5f illustrates the mechanism by which GF-IDE enhances humidity sensing performance. Briefly, water molecules permeate the ultrathin GO layer and accumulate between the electrode and the humidity-sensitive material. Under the influence of an electric field, hydrogen ions undergo directional migration, thereby enhancing the humidity response. Furthermore, EIS measurements across varying humidity levels (Fig. S26 and Fig. 5g) elucidate the underlying sensing mechanism: at low humidity, water molecules undergo chemisorption onto the oxygen-containing functional groups of GO, preventing the formation of a continuous water layer and hindering ionic conduction, resulting in extremely high impedance. As humidity increases, a physisorbed water layer covers the chemisorbed monolayer. This continuous water film facilitates H_3O^+ ion transport, leading to a significant reduction in impedance. At high humidity regimes: Physisorption approaches saturation, with multiple water layers covering the surface. Proton conduction proceeds predominantly via the Grotthuss mechanism (sequential proton hopping between adjacent water molecules).

To evaluate its application potential, the GF-GO sensor was deployed in human breath monitoring and contactless human-machine interaction. For contactless button operation, the sensor responds to signals by detecting ambient humidity changes induced by a finger, effectively eliminating the need for direct contact and thereby significantly mitigating the risk of pathogen cross-transmission. Human skin continuously releases moisture through sweat evaporation. As demonstrated in Figs. 6a and b, when a finger approaches the sensor surface, water molecules are adsorbed by the GO humidity-sensitive layer, leading to a substantial increase in electrical conductivity and a corresponding significant decrease in impedance. As the finger gradually moves away (from 1 mm to 5 mm), the impedance value rises accordingly. Crucially, distinct distances correspond to specific impedance values, exhibiting an excellent linear relationship between distance and impedance (Fig. 6c).

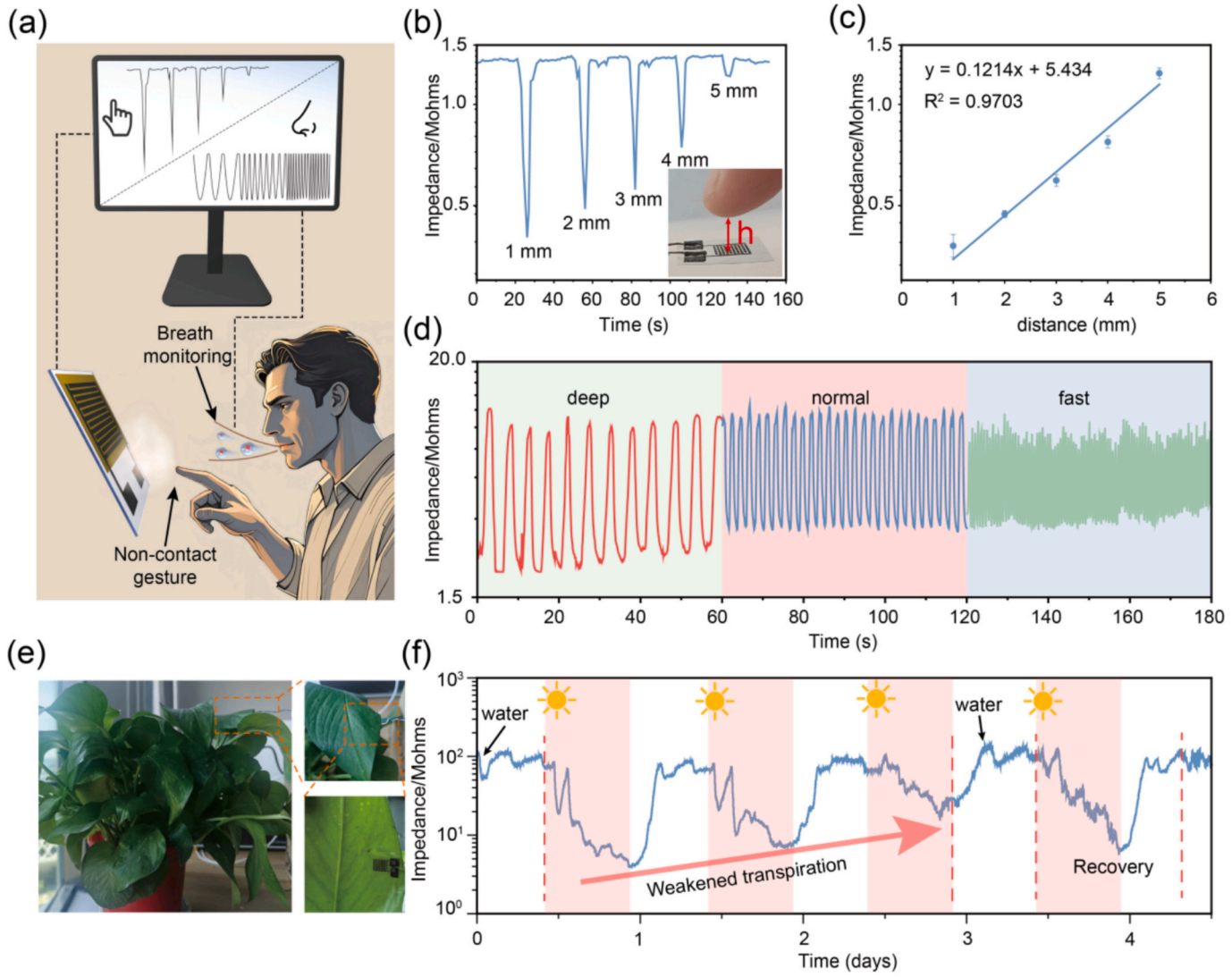

Fig. 6. (a) Schematic illustration of the GF-GO sensor applied in non-contact human-machine interaction and respiration monitoring. (b) Impedance response at different contact distances and (c) its linear correlation characteristics. (d) Impedance response of the GF-GO sensor to different breathing patterns. (e) Optical photograph of the GF-GO sensor installed on the abaxial surface (underside) of a plant leaf. (f) Real-time impedance-time curve monitoring the transpiration process of a plant using the GF-GO sensor.

Furthermore, integrated into a face mask, the sensor leverages its humidity responsiveness to track respiratory rate and depth in real-time, providing crucial data for disease pre-warning and health management. Fig. 6d clearly illustrates the sensor's real-time response curves to three distinct breathing patterns: rapid breathing (90 breaths/min), normal breathing (27 breaths/min), and deep breathing (11 breaths/min). Beyond frequency, the sensor also effectively responds to variations in breathing depth: the impedance change amplitude is greatest during deep breathing and smallest during rapid breathing. Table S3 quantifies the sensing data of the GF-GO sensor for human breath monitoring. These results collectively demonstrate the reliable and sensitive response of the sensor to both finger proximity/distance and diverse breathing patterns, highlighting the dual application potential of the GF-GO sensor in healthcare monitoring and contactless human-machine interaction interfaces.

Furthermore, plant transpiration, serving as a critical water regulation mechanism, is closely linked to plant growth and physiological processes [2]. Typically, the density of stomata on the lower leaf surface exceeds that on the upper surface, and the frequency of stomatal distribution is higher in the upper regions of the stem morphology [60]. Building on this understanding, a GF-GO sensor was integrated onto the upper stem region (Fig. 6e) to monitor humidity changes primarily associated with the lower leaf surface, thereby enabling the tracking of dynamic plant transpiration patterns. Fig. 6f illustrates the transpiration variation curve of a plant over four consecutive day-night cycles: the plant was normally watered the night before testing commenced, followed by three days of simulated drought conditions. The results reveal that transpiration peaked during the afternoon of the first day, began to decline on the second day, and exhibited a further significant reduction on the third day compared to the second day (manifested as an increase in impedance value). Upon resuming normal watering on the evening of the third day, the daytime transpiration level on the fourth day recovered to a level comparable to that of the first day.

Conventional plant sensors still rely on metallic substrates for electrodes, which lack long-term durability under extreme conditions, such as high salinity or alkaline environments. In contrast, the sensor developed in this work exhibits exceptional stability in harsh settings—including salt spray and alkaline conditions—making it suitable for deployment in saline-alkaline soils and coastal agricultural areas. These findings collectively demonstrate the efficacy of the GF-GO humidity sensor in dynamically monitoring plant transpiration. This capability highlights its considerable promise for applications in plant

physiological research and precision agriculture growth monitoring.

5. Conclusion

In summary, this work successfully overcomes the limitations of conventional electrode substrates by developing a scalable, high-performance graphene film (GF) through thermal annealing and roller pressing. The resulting GF exhibits exceptional electrical conductivity, remarkable flexibility, and superior environmental stability, enabling its use as a robust electrode substrate for humidity sensors. By integrating a conformal graphene oxide sensing layer, an all-carbon humidity sensor was constructed, demonstrating high sensitivity, fast response/recovery, and outstanding durability under mechanical bending and harsh environmental conditions. The GF-based platform not only offers a viable alternative to traditional metal and LIG electrodes but also opens up broad applications in wearable health monitoring, non-contact human-machine interfaces, and precision agriculture. This study provides a scalable and efficient strategy for designing next-generation sensing devices with enhanced environmental adaptability and mechanical reliability.

Supplementary data to this article can be found online at https://doi.org/10.1016/j.cej.2025.169730.

CRediT authorship contribution statement

Zhenyu Gong: Writing – original draft, Visualization, Resources, Methodology, Investigation. **Zibo Chen:** Writing – original draft, Methodology, Formal analysis. **Fangzheng Xi:** Visualization, Software, Investigation. **Bo Liu:** Writing – review & editing, Supervision, Project administration, Formal analysis, Conceptualization. **Yunfa Si:** Methodology, Formal analysis. **Jie Wen:** Validation, Software, Methodology. **Xiaodong Ji:** Visualization, Software. **Mingyang Tanwei:** Methodology, Investigation. **Cheng Chen:** Formal analysis. **Peng Li:** Methodology. **Shaowen Cao:** Supervision. **Geng Wu:** Writing – review & editing, Supervision, Resources, Funding acquisition, Formal analysis. **Daping He:** Writing – review & editing, Supervision, Resources, Project administration, Funding acquisition, Conceptualization.

Declaration of competing interest

The authors declare that they have no known competing financial interests or personal relationships that could have appeared to influence the work reported in this paper.

Acknowledgements

The authors sincerely acknowledge financial support from the National Natural Science Foundation of China (22279097, 22301287), Hainan Provincial Sanya Yazhou Bay Science and Technology Innovation Joint Project (No:ZDYF2025GXJS130) and the PhD Scientific Research and Innovation Foundation of The Education Department of Hainan Province Joint Project of Sanya Yazhou Bay Science and Technology City (HSPHDSRF-2024-03-022). The authors also acknowledge the Institutional Center for Shared Technologies and Facilities of IDSSE, CAS, for the help from the intermediate engineers, Dongmei Wang and Shuang Liu.

Data availability

Data will be made available on request.

References

[1] Y. Luo, J. Li, Q. Ding, H. Wang, C. Liu, J. Wu, Functionalized hydrogel-based wearable gas and humidity sensors, Nano-Micro Lett. 15 (2023) 136, https://doi.org/10.1007/s40820-023-01109-2.

[2] L. Huang, X. He, J. Hu, C. Qin, C. Huang, Y. Tang, F. Zhong, X. Kong, X. Wei, Wearable sensor based on covalent organic framework humidity films for long-term monitoring of tomato physiology under abiotic stress, ACS Nano 18 (2024) 33105–33118, https://doi.org/10.1021/acsnano.4c09916.

[3] S. Li, Y. Zhang, X. Liang, H. Wang, H. Lu, M. Zhu, H. Wang, M. Zhang, X. Qiu, Y. Song, Y. Zhang, Humidity-sensitive chemoelectric flexible sensors based on metal-air redox reaction for health management, Nat. Commun. 13 (2022) 5416, https://doi.org/10.1038/s41467-022-33133-y.

[4] L. Chen, K. Hu, M. Lu, Z. Chen, X. Chen, T. Zhou, X. Liu, W. Yin, C. Casiraghi, X. Song, Wearable sensors for breath monitoring based on water-based hexagonal boron nitride inks made with supramolecular functionalization, Adv. Mater. 36 (2024) 2312621, https://doi.org/10.1002/adma.202312621.

[5] P. Guo, B. Tian, J. Liang, X. Yang, G. Tang, Q. Li, Q. Liu, K. Zheng, X. Chen, W. Wu, An all-printed, fast-response flexible humidity sensor based on hexagonal-WO_3 nanowires for multifunctional applications, Adv. Mater. 35 (2023) 2304420, https://doi.org/10.1002/adma.202304420.

[6] Y. Liu, X. Li, H. Yang, P. Zhang, P. Wang, Y. Sun, F. Yang, W. Liu, Y. Li, Y. Tian, S. Qian, S. Chen, H. Cheng, X. Wang, Skin-interfaced superhydrophobic insensible sweat sensors for evaluating body thermoregulation and skin barrier functions, ACS Nano 17 (2023) 5588–5599, https://doi.org/10.1021/acsnano.2c11267.

[7] Y. Lu, G. Yang, Y. Shen, H. Yang, K. Xu, Multifunctional flexible humidity sensor systems towards noncontact wearable electronics, Nano-Micro Lett. 14 (2022) 150, https://doi.org/10.1007/s40820-022-00895-5.

[8] Y. Zu, Z. Duan, Z. Yuan, Y. Jiang, H. Tai, Electrospun nanofiber-based humidity sensors: materials, devices, and emerging applications, J. Mater. Chem. A 12 (2024) 27157–27179, https://doi.org/10.1039/D4TA05042H.

[9] A. Mei, W. Chen, Z. Yang, M. Zhou, W. Jin, S. Yang, K. Chen, Y. Liu, Study of intermolecular reconfiguration of flexible COF-5 film and its ultra-high chemiresistive humidity sensitivity, Angew. Chem. Int. Ed. 62 (2023) e202301440, https://doi.org/10.1002/ange.202301440.

[10] V. Montes-García, P. Samorì, Humidity sensing with supramolecular nanostructures, Adv. Mater. 35 (2023) 2208766, https://doi.org/10.1002/adma.202208766.

[11] T. Li, T. Zhao, H. Zhang, L. Yuan, C. Cheng, J. Dai, L. Xue, J. Zhou, H. Liu, L. Yin, J. Zhang, A skin-conformal and breathable humidity sensor for emotional mode recognition and non-contact human-machine interface, NPJ Flex. Electron. 8 (2024) 3, https://doi.org/10.1038/s41528-023-00290-z.

[12] S. Mandal, H.M. Mantilla, K. Loganathan, H. Faber, A. Sharma, M. Gedda, E. Yengel, D.K. Goswami, M. Heeney, T.D. Anthopoulos, Ultra-fast moisture sensor for respiratory cycle monitoring and non-contact sensing applications, Adv. Mater. (2024) 2414005, https://doi.org/10.1002/adma.202414005.

[13] L.-X. Liu, W. Chen, H.-B. Zhang, Q.-W. Wang, F. Guan, Z.-Z. Yu, Flexible and multifunctional silk textiles with biomimetic leaf-like MXene/silver nanowire nanostructures for electromagnetic interference shielding, humidity monitoring, and self-derived hydrophobicity, Adv. Funct. Mater. 29 (2019) 1905197, https://doi.org/10.1002/adfm.201905197.

[14] X. Zheng, S. Zhang, M. Zhou, H. Lu, S. Guo, Y. Zhang, C. Li, S.C. Tan, MXene functionalized, highly breathable and sensitive pressure sensors with multi-layered porous structure, Adv. Funct. Mater. 33 (2023) 2214880, https://doi.org/10.1002/adfm.202214880.

[15] S.T. Skowron, I.V. Lebedeva, A.M. Popov, E. Bichoutskaia, Energetics of atomic scale structure changes in graphene, Chem. Soc. Rev. 44 (2015) 3143–3176, https://doi.org/10.1039/C4CS00499J.

[16] Y. Fei, Y. Fu, X. Bai, L. Du, Z. Li, H. Komber, K.-H. Low, S. Zhou, D.L. Phillips, X. Feng, J. Liu, Defective nanographenes containing seven-five-seven (7-5-7)-membered rings, J. Am. Chem. Soc. 143 (2021) 2353–2360, https://doi.org/10.1021/jacs.0c12116.

[17] B. Liu, M. Chen, X. Liu, R. Fu, Y. Zhao, Y. Duan, L. Zhang, Bespoke tailoring of graphenoid sheets: a rippled molecular carbon comprising cyclically fused nonbenzenoid rings, J. Am. Chem. Soc. 145 (2023) 28137–28145, https://doi.org/10.1021/jacs.3c10303.

[18] W. Kong, H. Kum, S.-H. Bae, J. Shim, H. Kim, L. Kong, Y. Meng, K. Wang, C. Kim, J. Kim, Path towards graphene commercialization from lab to market, Nat. Nanotechnol. 14 (2019) 927–938, https://doi.org/10.1038/s41565-019-0555-2.

[19] T. Cui, S. Mukherjee, P.M. Sudeep, G. Colas, F. Najafi, J. Tam, P.M. Ajayan, C. V. Singh, Y. Sun, T. Filleter, Fatigue of graphene, Nat. Mater. 19 (2020) 405–411, https://doi.org/10.1038/s41563-019-0586-y.

[20] M. Zhao, Z. Zhang, W. Shi, Y. Li, C. Xue, Y. Hu, M. Ding, Z. Zhang, Z. Liu, Y. Fu, C. Liu, M. Wu, Z. Liu, X.-Z. Li, Z.-J. Wang, K. Liu, Enhanced copper anticorrosion from Janus-doped bilayer graphene, Nat. Commun. 14 (2023) 7447, https://doi.org/10.1038/s41467-023-43357-1.

[21] A. Zarepour, S. Ahmadi, N. Rabiee, A. Zarrabi, S. Iravani, Self-healing MXene- and graphene-based composites: properties and applications, Nano-Micro Lett. 15 (2023) 100, https://doi.org/10.1007/s40820-023-01074-w.

[22] J. Liu, Z. Tong, F. Gao, J. Wang, J. Hu, L. Song, Y. Hou, J. Lu, X. Zhan, Q. Zhang, Pearl-inspired intelligent marine hetero nanocomposite coating based on "brick&mortar" strategy: anticorrosion durability and switchable antifouling, Adv. Mater. 36 (2024) 2401982, https://doi.org/10.1002/adma.202401982.

[23] X. Xu, D. Yi, Z. Wang, J. Yu, Z. Zhang, R. Qiao, Z. Sun, Z. Hu, P. Gao, H. Peng, Z. Liu, D. Yu, E. Wang, Y. Jiang, F. Ding, K. Liu, Greatly enhanced anticorrosion of cu by commensurate graphene coating, Adv. Mater. 30 (2018) 1702944, https://doi.org/10.1002/adma.201702944.

[24] J. Ding, H. Zhao, H. Yu, Bio-inspired multifunctional graphene-epoxy anticorrosion coatings by low-defect engineered graphene, ACS Nano 16 (2022) 710–720, https://doi.org/10.1021/acsnano.1c08228.

[25] Y.-T. Kwon, Y.-S. Kim, S. Kwon, M. Mahmood, H.-R. Lim, S.-W. Park, S.-O. Kang, J. J. Choi, R. Herbert, Y.C. Jang, Y.-H. Choa, W.-H. Yeo, All-printed nanomembrane wireless bioelectronics using a biocompatible solderable graphene for multimodal human-machine interfaces, Nat. Commun. 11 (2020) 3450, https://doi.org/10.1038/s41467-020-17288-0.
[26] D. Kireev, S. Liu, H. Jin, T.P. Xiao, C.H. Bennett, D. Akinwande, J.A.C. Incorvia, Metaplastic and energy-efficient biocompatible graphene artificial synaptic transistors for enhanced accuracy neuromorphic computing, Nat. Commun. 13 (2022) 4386, https://doi.org/10.1038/s41467-022-32078-6.
[27] B.E. Hasanov, J. Casanova-Chafer, G. Deokar, J.D. Gouveia, S. Nematulloev, J.R. B. Gomes, E. Llobet, P.M.F.J. Costa, Amplified sensing of nitrogen dioxide with a phosphate-doped reduced graphene oxide powder, Carbon 226 (2024) 119207, https://doi.org/10.1016/j.carbon.2024.119207.
[28] Y.H. Kim, B.H. Park, Y.J. Choi, G.-W. Lee, H.-K. Kim, K.-B. Kim, Compact graphene powders with high volumetric capacitance: microspherical assembly of graphene via surface modification using cyanamide, Energy Storage Mater. 24 (2020) 351–361, https://doi.org/10.1016/j.ensm.2019.07.039.
[29] N. Samartzis, M. Athanasiou, V. Dracopoulos, S.N. Yannopoulos, T. Ioannides, Laser-assisted transformation of a phenol-based resin to high quality graphene-like powder for supercapacitor applications, Chem. Eng. J. 430 (2022) 133179, https://doi.org/10.1016/j.cej.2021.133179.
[30] P. Li, M. Yang, Y. Liu, H. Qin, J. Liu, Z. Xu, Y. Liu, F. Meng, J. Lin, F. Wang, C. Gao, Continuous crystalline graphene papers with gigapascal strength by intercalation modulated plasticization, Nat. Commun. 11 (2020) 2645, https://doi.org/10.1038/s41467-020-16494-0.
[31] J. Wang, N. Wang, D. Xu, L. Tang, B. Sheng, Flexible humidity sensors composed with electrodes of laser induced graphene and sputtered sensitive films derived from poly(ether-ether-ketone), Sensors Actuators B Chem. 375 (2023) 132846, https://doi.org/10.1016/j.snb.2022.132846.
[32] S. Zou, L.-Q. Tao, G. Wang, C. Zhu, Z. Peng, H. Sun, Y. Li, Y. Wei, T.-L. Ren, Humidity-based human-machine interaction system for healthcare applications, ACS Appl. Mater. Interfaces 14 (2022) 9397–9406, https://doi.org/10.1021/acsami.1c23725.
[33] L. Lan, X. Le, H. Dong, J. Xie, Y. Ying, J. Ping, One-step and large-scale fabrication of flexible and wearable humidity sensor based on laser-induced graphene for real-time tracking of plant transpiration at bio-interface, Biosens. Bioelectron. 165 (2020) 112360, https://doi.org/10.1016/j.bios.2020.112360.
[34] L. Chen, N. Li, X. Yu, S. Zhang, C. Liu, Y. Song, Z. Li, S. Han, W. Wang, P. Yang, N. Hong, S. Ali, Z. Wang, A general way to manipulate electrical conductivity of graphene, Chem. Eng. J. 462 (2023) 142139, https://doi.org/10.1016/j.cej.2023.142139.
[35] L. Wang, K. Yin, X. Li, Y. Huang, J. Xiao, J. Pei, X. Song, J.-A. Duan, C.J. Arnusch, Femtosecond laser ultrafast atomic scale renovating laser-induced graphene, Adv. Funct. Mater. (2025) 2506215, https://doi.org/10.1002/adfm.202506215.
[36] B. Fang, S.C. Bodepudi, F. Tian, X. Liu, D. Chang, S. Du, J. Lv, J. Zhong, H. Zhu, H. Hu, Y. Xu, Z. Xu, W. Gao, C. Gao, Bidirectional mid-infrared communications between two identical macroscopic graphene fibres, Nat. Commun. 11 (2020) 6368, https://doi.org/10.1038/s41467-020-20033-2.
[37] Z. Lin, J. Dong, X. Wang, Q. Huang, X. Shen, M. Yang, X. Sun, Y. Yuan, S. Wang, Y. Ning, S. Yang, W. Yin, M. Li, Y. Sun, Q. Zhang, Y. Li, Twin-structured graphene metamaterials with anomalous mechanical properties, Adv. Mater. 34 (2022) 2200444, https://doi.org/10.1002/adma.202200444.
[38] Z. Wu, C. Xu, C. Ma, Z. Liu, H.-M. Cheng, W. Ren, Synergistic effect of aligned graphene nanosheets in graphene foam for high-performance thermally conductive composites, Adv. Mater. 31 (2019) 1900199, https://doi.org/10.1002/adma.201900199.
[39] C.E. Halbig, B. Mukherjee, S. Eigler, S. Garaj, Origin of oxygen in graphene oxide revealed by 17O and 18O isotopic labeling, J. Am. Chem. Soc. 146 (2024) 7431–7438, https://doi.org/10.1021/jacs.3c12543.
[40] H. Fu, B. Wang, D. Zhu, Z. Zhou, S. Bao, X. Qu, Y. Guo, L. Ling, S. Zheng, P. Duan, J. Mao, K. Schmidt-Rohr, S. Tao, P.J.J. Alvarez, Mechanism for selective binding of aromatic compounds on oxygen-rich graphene nanosheets based on molecule size/polarity matching, Sci. Adv. 8 (2022) eabn4650, https://doi.org/10.1126/sciadv.abn4650.
[41] M. Huang, C. Wang, L. Quan, T.H.-Y. Nguyen, H. Zhang, Y. Jiang, G. Byun, R. S. Ruoff, CVD growth of porous graphene foam in film form, Matter 3 (2020) 487–497, https://doi.org/10.1016/j.matt.2020.06.012.
[42] S. Sy, G. Jiang, J. Zhang, H. Zarrin, T. Cumberland, S. Abureden, E. Bell, J. Gostick, A. Yu, Z. Chen, A near-isotropic proton-conducting porous graphene oxide membrane, ACS Nano 14 (2020) 14947–14959, https://doi.org/10.1021/acsnano.0c04533.
[43] Z. Wang, Q. Yao, C. Neumann, F. Börrnert, J. Renner, U. Kaiser, A. Turchanin, H.J. W. Zandvliet, S. Eigler, Identification of semiconductive patches in thermally processed monolayer oxo-functionalized graphene, Angew. Chem. Int. Ed. 59 (2020) 12693–12697, https://doi.org/10.1002/anie.202004005.
[44] R. Si, X. Xie, T. Li, J. Zheng, C. Cheng, S. Huang, C. Wang, TiO2/(K,Na)NbO3 nanocomposite for boosting humidity-sensing performances, ACS Sens. 5 (2020) 1345–1353, https://doi.org/10.1021/acssensors.9b02586.
[45] Y. Liang, Q. Ding, H. Wang, Z. Wu, J. Li, Z. Li, K. Tao, X. Gui, J. Wu, Humidity sensing of stretchable and transparent hydrogel films for wireless respiration monitoring, Nano-Micro Lett. 14 (2022) 183, https://doi.org/10.1007/s40820-022-00934-1.
[46] M.A. Andrés, M.T. Vijjapu, S.G. Surya, O. Shekhah, K.N. Salama, C. Serre, M. Eddaoudi, O. Roubeau, I. Gascón, Methanol and humidity capacitive sensors based on thin films of MOF nanoparticles, ACS Appl. Mater. Interfaces 12 (2020) 4155–4162, https://doi.org/10.1021/acsami.9b20763.
[47] Y. Zhang, W. Zhang, Q. Li, C. Chen, Z. Zhang, Design and fabrication of a novel humidity sensor based on ionic covalent organic framework, Sensors Actuators B Chem. 324 (2020) 128733, https://doi.org/10.1016/j.snb.2020.128733.
[48] W. Waheed, S. Anwer, M.U. Khan, M. Sajjad, A. Alazzam, 2D $Ti_3C_2T_x$-MXene nanosheets and graphene oxide based highly sensitive humidity sensor for wearable and flexible electronics, Chem. Eng. J. 480 (2024) 147981, https://doi.org/10.1016/j.cej.2023.147981.
[49] M.U. Khan, Y. Abbas, H. Abunahla, M.D. Rezeq, A. Alazzam, N. Alamoodi, B. Mohammad, Biocompatible humidity sensor using paper cellulose fiber/GO matrix for human health and environment monitoring, Sensors Actuators B Chem. 393 (2023) 134188, https://doi.org/10.1016/j.snb.2023.134188.
[50] L. Li, J. Zhang, Y. Song, R. Dan, X. Xia, J. Zhao, R. Xu, Flexible humidity sensor based on a graphene oxide-carbon nanotube-modified Co_3O_4 nanoparticle-embedded laser-induced graphene electrode, ACS Appl. Mater. Interfaces 16 (2024) 33981–33992, https://doi.org/10.1021/acsami.4c05993.
[51] X. Le, Y. Liu, L. Peng, J. Pang, Z. Xu, C. Gao, J. Xie, Surface acoustic wave humidity sensors based on uniform and thickness controllable graphene oxide thin films formed by surface tension, Microsyst. Nanoeng. 5 (2019) 36, https://doi.org/10.1038/s41378-019-0075-0.
[52] S.Y. Park, J.E. Lee, Y.H. Kim, J.J. Kim, Y.-S. Shim, S.Y. Kim, M.H. Lee, H.W. Jang, Room temperature humidity sensors based on rGO/MoS_2 hybrid composites synthesized by hydrothermal method, Sensors Actuators B Chem. 258 (2018) 775–782, https://doi.org/10.1016/j.snb.2017.11.176.
[53] X. Yu, S. Ma, D. Long, W. Li, X. Yu, X. Ding, Investigation of the influence of GO size on the humidity sensing performance, Sensors Actuators B Chem. 429 (2025) 137286, https://doi.org/10.1016/j.snb.2025.137286.
[54] X. Yu, X. Chen, X. Ding, K. Tang, F. Liu, J. Lu, High-response humidity sensor based on silicon microbridge with edge-constrained sandwich sensing structure, Sensors Actuators B Chem. 413 (2024) 135858, https://doi.org/10.1016/j.snb.2024.135858.
[55] R. Zhang, B. Peng, Y. Yuan, Flexible printed humidity sensor based on poly(3,4-ethylenedioxythiophene)/reduced graphene oxide/au nanoparticles with high performance, Compos. Sci. Technol. 168 (2018) 118–125, https://doi.org/10.1016/j.compscitech.2018.09.013.
[56] T. Qin, Z. Yang, H. Fu, L. Zhao, Z. Yong, L. Chen, K. Wu, C. Li, C. Zhang, Y. Zhang, Y. Cao, H. Yu, D. Liu, Q. Li, Centrifugation-modulated uniform antibacterial paper with well-interconnected hierarchical pores for flexible high-sensitivity humidity monitoring, Chem. Eng. J. 500 (2024) 156824, https://doi.org/10.1016/j.cej.2024.156824.
[57] R. Zhao, D. Xie, S. Qing, B. Zhu, W. Shen, L. Wang, X. Meng, J. Pang, Cellulose acetate and reduced graphene oxide (rGO)-based flexible humidity sensor for monitoring human respiration, Sensors Actuators B Chem. 429 (2025) 137291, https://doi.org/10.1016/j.snb.2025.137291.
[58] Z.-H. Duan, Q.-N. Zhao, C.-Z. Li, S. Wang, Y.-D. Jiang, Y.-J. Zhang, B.-H. Liu, H.-L. Tai, Enhanced positive humidity sensitive behavior of p-reduced graphene oxide decorated with n-WS_2 nanoparticles, Rare Met. 40 (2021) 1762–1767, https://doi.org/10.1007/s12598-020-01524-z.
[59] H. Huang, H. Park, J. Huang, Self-crosslinking of graphene oxide sheets by dehydration, Chem 8 (2022) 2432–2441, https://doi.org/10.1016/j.chempr.2022.05.016.
[60] L. Huang, Y. Cai, P. Huang, Z. Liao, Y. Tang, J. Pang, X. Kong, X. Wei, Covalent self-assembled highly sensitive humidity sensing system with wireless communication for plant physiology perception under disease stress, Chem. Eng. J. 518 (2025) 164501, https://doi.org/10.1016/j.cej.2025.164501.